



A Stokesian viscoelastic flow: Transition to oscillations and mixing

Becca Thomases^{a,*}, Michael Shelley^b, Jean-Luc Thiffeault^c

^a Department of Mathematics, University of California, Davis, CA 95616, United States

^b Courant Institute of Mathematical Sciences, New York University, New York City, NY 10012, United States

^c Department of Mathematics, University of Wisconsin Madison, WI 53706, United States

ARTICLE INFO

Article history:

Available online 25 June 2011

Keywords:

Viscoelasticity
Instability
Mixing
Microfluidics

ABSTRACT

To understand observations of low Reynolds number mixing and flow transitions in viscoelastic fluids, we study numerically the dynamics of the Oldroyd-B viscoelastic fluid model. The fluid is driven by a simple time-independent forcing that, in the absence of viscoelastic stresses, creates a cellular flow with extensional stagnation points. We find that at $\mathcal{O}(1)$ Weissenberg number, these flows lose their slaving to the forcing geometry of the background force, become oscillatory with multiple frequencies, and show continual formation and destruction of small-scale vortices. This drives flow mixing, the details of which we closely examine. These new flow states are dominated by a single-quadrant vortex, which may be stationary or cycle persistently from cell to cell.

© 2011 Elsevier B.V. All rights reserved.

1. Introduction

In the past several years, it has come to be appreciated that in low Reynolds number flow the nonlinearities provided by non-Newtonian stresses of a complex fluid can provide rich dynamical behaviors more commonly associated with high Reynolds number Newtonian flow. For example, experiments by Steinberg and collaborators have shown that dilute polymer suspensions being sheared in simple flow geometries can exhibit highly time-dependent dynamics and efficient mixing [1–3]. The corresponding experiments using Newtonian fluids do not – and indeed cannot – show such nontrivial dynamics. One important constraint on the dynamics of a Stokesian Newtonian fluid is reversibility [4], which is lost when the fluid is viscoelastic [5,6].

Both mixing and irreversibility are complex phenomena but even the understanding of elastic instabilities in viscoelastic fluids is incomplete. Elastic instabilities in low Reynolds number fluids, where inertia is negligible, have been studied extensively for some time; see [7–14]. Elastic instabilities are observed at low or modest flow rates where inertial forces are negligible but elastic forces are strong, and have been linked to the creation of secondary vortex flows [15] and increased flow resistance [16].

Extensional flows, such as the flow in a four-roll mill or flow in a cross-channel, can be more effective in locally stretching and aligning polymers than a standard shear flow [17]. As the macroscopic flow depends on the microscopically generated

stresses, a flow in an extensional geometry may exhibit an instability more readily than a flow in a shearing geometry. This may be due to the fact that a shear flow can be decomposed into an extensional flow and a rotational flow and the vorticity in the fluid tends to rotate the fluid microstructure away from the principal axes of stretching [18,13]. Experiments have shown that polymer molecules are strongly stretched as they pass near extensional points in a micro-channel cross flow [19,20]. Schroeder et al. [19] visualized single-molecule stretching and bistability at stagnation points. In the work of Arratia et al. [20], molecular stretching is inferred and two flow instabilities, dependent on the flow strain rate, are demonstrated. After the onset of the first instability, the flow becomes deformed and asymmetric but remains steady; at higher strain rates the velocity field fluctuates in time and can produce mixing. The first transition appears to be a forward bifurcation to a bistable steady state; see also [21,22]. In [23], (henceforth TS2009) these instabilities are demonstrated numerically for a 2D periodic flow, and these results are discussed in greater detail here. Xi and Graham [24] also found numerically an oscillatory instability for sufficiently large Weissenberg number in an extensional flow geometry, and they suggest a possible mechanism for the instability due to the concentration of stress near the extensional point in the flow. In [25], Berti et al. show numerically that flows with a 2D periodic shearing force can give rise to non-stationary dynamics.

In this paper, we study computationally a viscoelastic fluid in an extensional flow. As our flow model, we use the Oldroyd-B equations with polymer stress diffusion in the zero Reynolds number (Stokes) limit. The Stokes–Oldroyd-B model is attractive as it arises from a simple conception of the microscopic origin of viscoelasticity [26,27]. The bulk fluid is composed of a Newtonian

* Corresponding author. Tel.: +1 5305542988; fax: +1 5307526635.
E-mail address: thomases@math.ucdavis.edu (B. Thomases).

(Stokesian) solvent with a dilute concentration of immersed polymer chains, themselves modeled as Hookean springs. The polymer stress is proportional to the second moment of the configuration distribution function. One consequence of modeling the response of a polymer coil as a linear Hookean spring is that the Oldroyd-B equations put no limit on the deformed length of a stretched coil. This yields unphysical infinite viscosities at finite strain rates for viscometric straining flows [27]. In [28] this defect in the model was linked to the exponential growth of the polymer stress at extensional stagnation points in the flow; see also [29–32].

As part of the calibration of our model we compare it with the standard Stokes–Oldroyd-B model and the FENE-P model (a modification of the Oldroyd-B model which enforces a finite polymer extension length) for 2D periodic extensional flows (see Appendix B). We show that adding a small amount of polymer stress diffusion yields structures qualitatively similar to FENE-P while maintaining a bounded and smooth polymer stress field. This diffusion term is not added without physical justification, as some polymer stress diffusion can be justified from kinetic theory [26] and there are many other proposed models which seek to incorporate it; see for example [33–35].

In a previous study [28] (henceforth TS2007) Thomases and Shelley studied the standard Stokes–Oldroyd-B model in two dimensions. The relevant results from this study will be reviewed in Section 2. Here we add perturbations to the flows studied in TS2007 and look at the dynamics that are introduced. Our main observation is that for sufficiently large Weissenberg number the symmetric solutions obtained in TS2007 are not stable to asymmetric perturbations in the initial data. Rather, these perturbations induce a symmetry-breaking transition which will lead to asymmetric states that are qualitatively different in character from the symmetric solutions found in TS2007 and from solutions at small Weissenberg number.

Furthermore it is shown that this transition to an asymmetric state leads to enhanced mixing in the fluid across large regions of the flow domain. For low Weissenberg number flows the four-roll mill flow topology is preserved and hence fluid particles near distinct rollers do not mix. However, when the flow transitions to the asymmetric state and then to a state with higher-frequency time-dependent fluctuations there can be significant mixing.

In Section 2, the Stokes–Oldroyd-B equations with diffusion are described along with some basic properties. The numerical method used in the simulations is described in Appendix A, and the choice and calibration of our model is discussed in Appendix B. We discuss the transitions in Section 3. In Section 3.1 we provide a detailed look at the first symmetry-breaking transition. Section 3.2 gives results from perturbing the flow with initial data of random structure. There is a second transition which occurs in the flow (at higher Weissenberg number) and we conjecture an explanation for this second transition in Section 3.3. Section 4 is devoted to a discussion of mixing in the fluid, including both demonstrations of the phenomena and measures to quantify the level of mixing. We discuss the effective diffusion induced by the polymer stress in Section 4.2 and compute Lyapunov exponents in Section 4.3. Our conclusions and further directions are discussed in Section 5.

2. Background

The 2d Stokes–Oldroyd-B system with polymer stress diffusion is given in dimensionless form by:

$$-\nabla p + \Delta \mathbf{u} = -\beta \nabla \cdot \mathbf{S} + \mathbf{f}, \quad \nabla \cdot \mathbf{u} = 0, \quad (1)$$

$$\mathbf{S}^\nabla + (\text{Wi})^{-1}(\mathbf{S} - \mathbf{I}) = \nu_p \Delta \mathbf{S}, \quad (2)$$

where the upper convected time derivative, \mathbf{S}^∇ , is defined by

$$\mathbf{S}^\nabla \equiv \frac{\partial \mathbf{S}}{\partial t} + \mathbf{u} \cdot \nabla \mathbf{S} - (\nabla \mathbf{u} \cdot \mathbf{S} + \mathbf{S} \nabla \mathbf{u}^T). \quad (3)$$

The polymer stress, \mathbf{S} , is a symmetric positive definite 2-tensor and its trace ($S_{11} + S_{22}$) represents the mean-squared distension of polymer coils. The Weissenberg number is given by $\text{Wi} = \tau_p/\tau_f$, with τ_p the polymer relaxation time and τ_f a typical time-scale of the fluid flow. Here, our external force, \mathbf{f} , is used to drive the flow, and its dimensional scale F is used to set the flow time-scale as $\tau_f = \mu/\rho LF$, where μ is the solvent viscosity, ρ the fluid density, and L the system size. This sets the dimensionless force, and the time-scale of transport, to be order one. With the particular choice here for \mathbf{f} , τ_f^{-1} is also the strain rate of extensional stagnation points in the induced Newtonian flow, which explains our use of the Weissenberg number rather than the Deborah number for this discussion.

The parameter $\beta = G\tau_f/\mu$ measures the relative contribution of the polymer stress to the momentum balance, where G is the isotropic stress induced by the polymer field in the absence of flow. The parameter ν_p controls the polymer stress diffusion. Stress diffusion can arise when including the effect of center of mass diffusion of polymer coils [36]. Here it is added to control polymer stress gradient growth as Eqs. (1)–(2) otherwise lack a scale-dependent dissipation (see also [33–35] for other models incorporating stress diffusion). In the following simulations we fix $\nu_p = 10^{-3}$; the calibration of this parameter is discussed in Appendix B.

The quantity $\beta \cdot \text{Wi}$ is the ratio of the polymer viscosity to solvent viscosity, so that given a particular working fluid the ratio is fixed independent of experimental conditions. As a useful point of comparison, from the work of Arratia et al. [20] the solution viscosity is 1.2 Pa s, while the solvent (97% glycerol/water) is 0.8 Pa s, yielding $\beta \cdot \text{Wi} = (1.2 - 0.8)/0.8 = 0.5$. We keep the product $\beta \cdot \text{Wi} = 0.5$ in our simulations.

The Stokes–Oldroyd-B equations with polymer stress diffusion also have a relative strain energy for the distension of the polymer field:

$$\mathcal{E}(t) = \frac{1}{2} \int_{\Omega} \text{trace}(\mathbf{S} - \mathbf{I}) \, d\mathbf{x}, \quad (4)$$

which satisfies

$$\dot{\mathcal{E}} + \text{Wi}^{-1} \mathcal{E} = -\mathcal{D} + \mathcal{W}, \quad (5)$$

where

$$\mathcal{D} = \beta^{-1} \int |\nabla \mathbf{u}|^2 \, d\mathbf{x}$$

is the rate of viscous dissipation and

$$\mathcal{W} = -\beta^{-1} \int \mathbf{f} \cdot \mathbf{u} \, d\mathbf{x}$$

is the power input by the forcing. Note that for fixed β , $\mathcal{E}(t)$ will decay (for $\mathbf{f} \equiv 0$) even in the limit of infinite Wi owing to the viscous response of the Newtonian solvent.

The standard Stokes–Oldroyd-B equations are given by Eqs. (1)–(2) with $\nu_p = 0$. In this case, the Newtonian Stokes equations are recovered in the limit $\text{Wi} \rightarrow 0$, in which case the polymer stress is uniform and isotropic. In TS2007 the 2D Stokes–Oldroyd-B equations were simulated on a 2π -periodic domain, $[-\pi, \pi]^2$, with a steady background force of the form

$$\mathbf{f} = \begin{pmatrix} 2 \sin x \cos y \\ -2 \cos x \sin y \end{pmatrix}. \quad (6)$$

In a Newtonian Stokes flow with doubly periodic boundary conditions this yields the velocity field $\mathbf{u} = -\frac{1}{2}\mathbf{f}$, which is a four-roll mill flow with counter-rotating vortices of equal magnitude.

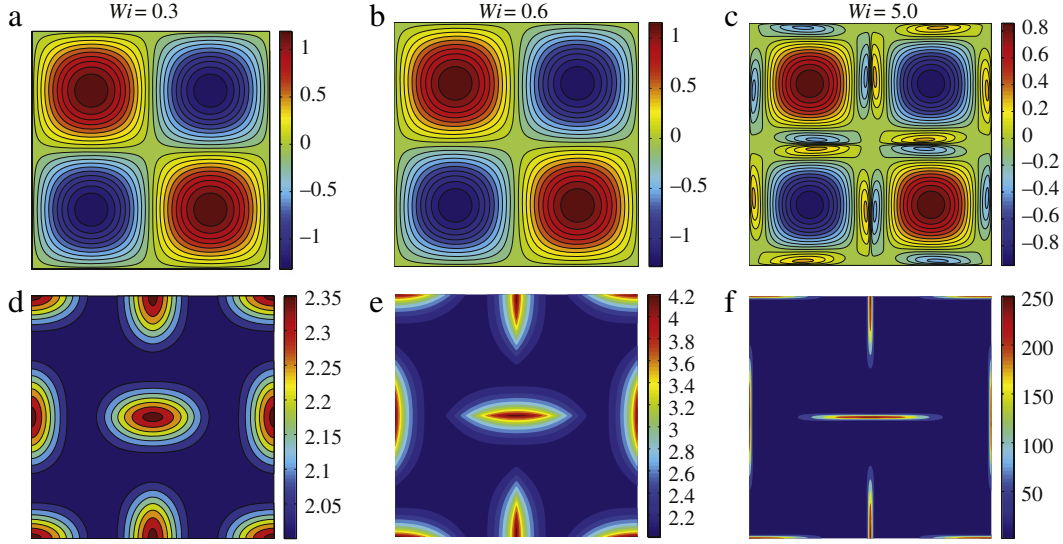


Fig. 1. Contour plots of components of velocity and polymer stress evolving from Stokes–Oldroyd-B equations without polymer stress diffusion and isotropic initial data at $t = 6$. (a)–(c) Vorticity for $Wi = 0.3, 0.6$, and 5 respectively. (d)–(f) $\text{tr } \mathbf{S}$ for $Wi = 0.3, 0.6$, and 5 respectively. From TS2007 with permission.

This forcing fixes an extensional stagnation point at the origin (and $(\pm\pi, 0)$, $(0, \pm\pi)$, and $(\pm\pi, \pm\pi)$). The stagnation points are maintained dynamically if the flow is not perturbed and the initial stress is isotropic, $\mathbf{S}(0) = \mathbf{I}$.

In TS2007 it was observed that for small Weissenberg number, $Wi < 0.5$, the polymer stress reaches a smooth steady state rapidly and the velocity field remains slaved to the background force; see Fig. 1(a). For $0.5 \lesssim Wi \lesssim 1$ the polymer stress converges exponentially in time to a solution which has a singularity in the first derivative, a cusp; see Fig. 1(e). However, the vorticity field is qualitatively unchanged by this emerging singularity; see Fig. 1(b). However, for sufficiently large Weissenberg number, $Wi \gtrsim 1$, the polymer stress diverges exponentially in time; see Fig. 1(f). The vorticity field is shown in Fig. 1(c) where we see that smaller oppositely signed vortices emerge along the incoming and outgoing streamlines of the extensional points in the flow.

The singular behavior in the polymer stress, and the critical values for the transitions, was confirmed by constructing a dynamical local solution which agrees very well with the simulations near the extensional point in the flow; see also [37,32]. For $Wi \gtrsim 1$, $\text{tr } \mathbf{S}$ concentrates on sets of exponentially decreasing measure along the streamlines associated with the extensional stagnation point, which may in part be why the velocity field appears to reach a steady state where the polymer stress field is diverging exponentially. With isotropic initial data for \mathbf{S} , the polymer stress and velocity field remain symmetric, in particular, the S_{22} field is a rotation and translation of the S_{11} field, $\text{tr } \mathbf{S}$ has 4-fold symmetry, and each component of the polymer stress and the vorticity have 2-fold symmetry.

3. Instabilities

3.1. Symmetry breaking

With isotropic initial data, $\mathbf{S}(0) = \mathbf{I}$, Eqs. (1)–(2) are simulated in a 2D periodic box $[-\pi, \pi]^2$ with steady background force \mathbf{f} given by (6). The system is solved by a pseudo-spectral method (see Appendix A for details). With $n^2 = 256^2$ grid-points, the high-wavenumber part of the spatial Fourier spectrum is $\mathcal{O}(10^{-12})$ throughout the simulations, and doubling the spatial resolution does not change the observed dynamics. For $Wi \leq 10$ and $v_p = 10^{-3}$ solutions converge to steady states which are reminiscent

of the solutions found in TS2007. The main difference is that the polymer stress is cut off by diffusion, and now saturates, with \mathbf{S} remaining smooth and bounded. Other features seen in the solutions from TS2007 (Fig. 1) are quite similar: $\text{tr } \mathbf{S}$ concentrates in symmetric “stress islands” along the outgoing streamlines of the flow. There is a coil-stretch transition which occurs around $Wi \approx 1$, beyond which $\text{tr } \mathbf{S}$ grows rapidly initially and additional oppositely signed vortices arise along the incoming and outgoing streamlines of extensional points in the flow, similar to those seen in Fig. 1(c) and (f).

To investigate the stability of these steady symmetric solutions we add small perturbations to symmetric steady solutions which have evolved from $\mathbf{S}(0) = \mathbf{I}$. We consider a state to be “converged” if $\max |\mathbf{S}(t+1) - \mathbf{S}(t)| < 10^{-7}$. For the symmetric solutions $S_{11}(x, y)$ is an even function of both x and y , so we introduce a small perturbation to the first odd Fourier mode in the y variable. The perturbation is $\mathcal{O}(0.05)$, and does not depend on the Weissenberg number or the extra stress diffusion. We focus on the first symmetry-breaking transition which occurs for $Wi \approx 4.8$. Here we try to pinpoint the critical value of Wi beyond which this symmetry breaking will occur and the rate at which it occurs. We plot the size of the perturbation in this mode as a function of time for each Wi . Fig. 2(a) shows the logarithm of the perturbation for $0 < t < 200$ for $Wi = 4.5, 4.6, 4.7, 4.8$, and 4.9 , while Fig. 2(b) shows the computed perturbation decay/growth rate. The transition from a decaying perturbation to a growing perturbation occurs between $Wi = 4.8$ and $Wi = 4.9$. There does appear to be a local maximum in the growth rate near $Wi = 9$.

Fig. 2(c) and (d) show components of the flow for $Wi = 5$ at $t = 1000$, as a result of this initial perturbation. Fig. 2(c) shows pathlines of the velocity field at a fixed time for some points located near the origin (the dot and dotted lines are at the origin, $x = 0$, and $y = 0$) and we see that the perturbation has caused the central stagnation point (CSP) to move into the upper half-plane, losing even symmetry in y . Similarly, Fig. 2(d) shows contour lines of $\text{tr } \mathbf{S}$ in the perturbed state, again having lost symmetry in the y -variable (the dotted lines are at $x = 0$ and $y = 0$). When the perturbation size is doubled or halved, the perturbation decay/growth rate does not change, nor does it change when the perturbation is made in a different Fourier mode. The transition Wi also does not depend on the size or location of the perturbation. When the perturbation is introduced in the x -variable, the CSP moves into the left half-plane, along the line $x = 0$, losing symmetry in this variable.

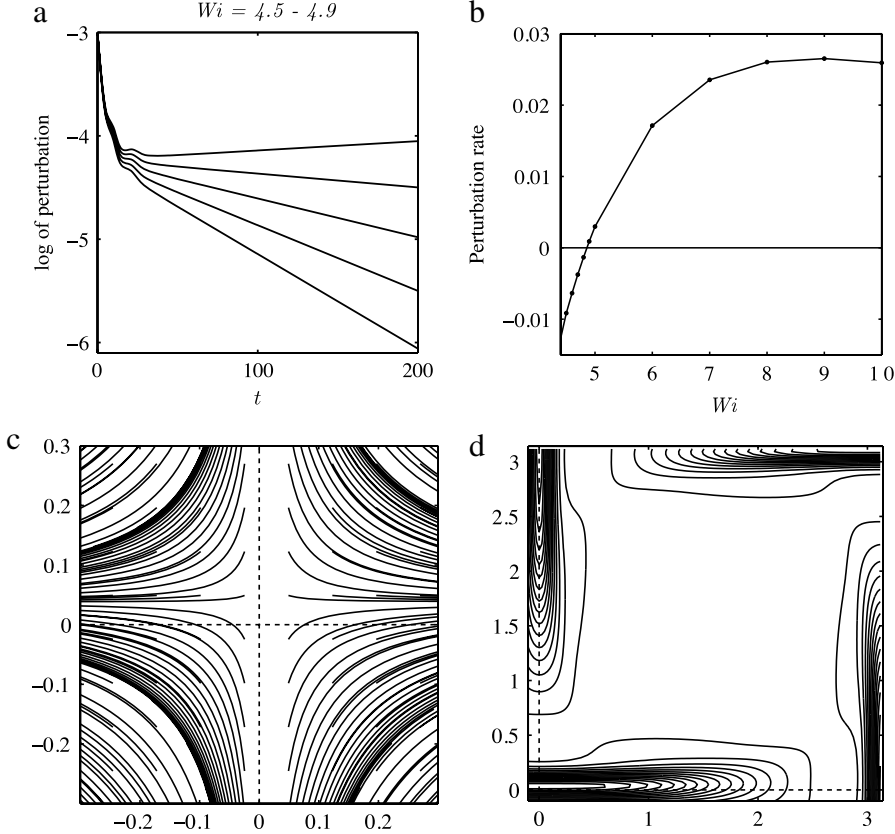


Fig. 2. (a) The logarithm of the perturbation over time for $Wi = 4.5$ (lowest curve), 4.6, 4.7, 4.8, and 4.9 (highest curve). The rate switches from decreasing to increasing between 4.8 and 4.9. (b) The perturbation rate as a function of Weissenberg number for $Wi \approx 4 - 10$. (c) and (d) Components of the velocity and polymer stress after evolving with the given perturbation for $Wi = 5$ at $t = 1000$. (c) Select pathlines of the velocity near $(0, 0)$ (d) Contour lines of $\text{tr } \mathbf{S}$ near $(0, 0)$.

3.2. Random initial data

To further investigate the stability of the symmetric solutions we evolve using initial data with random perturbations from isotropic initial polymer stress. Consider initial data of the form

$$\mathbf{S}(x, y, 0) = \mathbf{I} + \begin{pmatrix} \tilde{S}_{11}(x, y) & \tilde{S}_{12}(x, y) \\ \tilde{S}_{12}(x, y) & \tilde{S}_{22}(x, y) \end{pmatrix}. \quad (7)$$

Each \tilde{S}_{ij} ($i < j = 1, 2$) is a sum of 20 smooth periodic approximations to Gaussians of the form

$$\tilde{S}_{ij} = \sum_{k=1}^{20} c_k (1 + \sin(x - x_k))^{m_k} (1 + \sin(y - y_k))^{n_k},$$

where x_k, y_k are randomly distributed points in $[-\pi, \pi]$, m_k, n_k are randomly distributed in $[0, 100]$, and $c_k = (m_k + n_k)^{-1/2} 2^{-(m_k + n_k)}$ is a scaling factor to keep the size of the perturbation small. This will add 20 periodic near-Gaussian bumps of varying amplitude, location, and concentration to the initial polymer stress. The resultant effect on the velocity field is an $\mathcal{O}(10^{-3})$ perturbation from the four-roll mill geometry. For an example, a contour plot of the perturbation $\text{tr } \tilde{\mathbf{S}}$ is shown in Fig. 3(a) and a contour plot of the resultant perturbation to the vorticity is given in Fig. 3(b).

Fig. 4 shows the vorticity and polymer stress components both before and after the onset of a symmetry-breaking transition for $Wi = 10$. Solutions evolve from the random initial data shown in Fig. 3. Fig. 4(a)–(g) show these flow and stress components at $t = 100$ and demonstrate that the initial near-symmetry of the dynamics is maintained well into the evolution. Note that $\text{tr } \mathbf{S}$ is of much greater magnitude than S_{12} . At early times, $\text{tr } \mathbf{S}$ concentrates along the incoming and outgoing streamlines of the

extensional stagnation points in the flow, and oppositely signed vortices arise along these streamlines. At $t \approx 200$, a symmetry-breaking transition occurs, and the CSP, initially at the origin, migrates into the lower left quadrant. Fig. 4(b, e, h) show the flow and stress components at $t = 700$. In Fig. 4(b) we see that the vortex in the upper right quadrant is now dominant while the vortices in the remaining quadrants are much weaker. Fig. 4(e) and (h) show that the polymer stress has also reconfigured in an asymmetric manner, with the large stress islands in $\text{tr } \mathbf{S}$ surrounding the dominant vortex. Fig. 4(c)(f)(i) show the flow and stress components at $t = 1400$. Here the flow has become more complicated with some patches of negative vorticity in the lower left quadrant. The flow has undergone a second transition which will be discussed more fully in what follows.

For $Wi \lesssim 4.8$ the velocity remains slaved to the background forcing and perturbations in the initial data do not lead to a symmetry-breaking transition. Fig. 5(a) shows the velocity at a point in the flow (here $u = u_1(\pi/4, \pi/4)$) over $0 < t < 5000$ for $Wi = 5$ (upper curve), $Wi = 6$ (middle curve), and $Wi = 10$ (lower curve). Dynamically, what is observed for $Wi = 5$ is that the onset of the symmetry-breaking transition is quite slow, with the CSP slowly migrating into the upper right quadrant (the simulation shown here is for a different random initial configuration of the polymer stress). Fig. 5(c) shows select pathlines of the velocity well after the onset of the symmetry-breaking transition at $t = 3000$. This new state appears steady. For $Wi = 6$, the symmetry-breaking transition occurs more rapidly, with the CSP oscillating back and forth between the two upper quadrants. In Fig. 5(d) select pathlines of the velocity are shown for $Wi = 6$ at $t = 4000$ as the CSP settles on the line $x = 0$ in the upper half-plane. For $Wi = 10$, the situation is somewhat different. There is a more rapid symmetry-breaking transition again followed by oscillations in the velocity

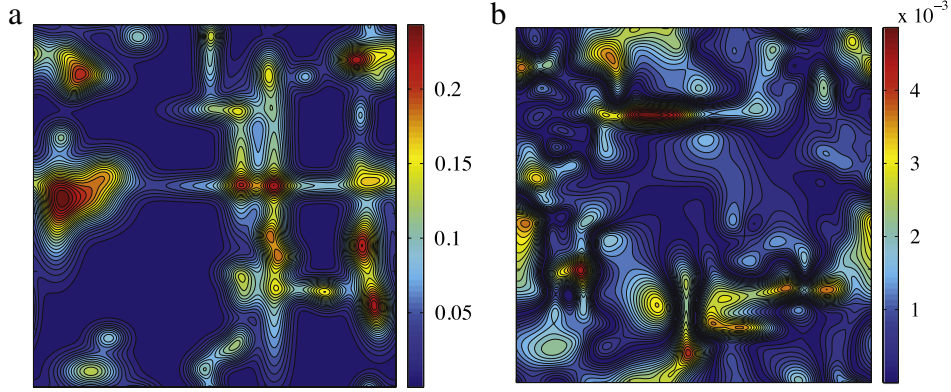


Fig. 3. (a) Contour plot of $\text{tr } \tilde{S}$, the perturbation from one random trial (b) Contour plot of the resultant perturbation to the vorticity field.

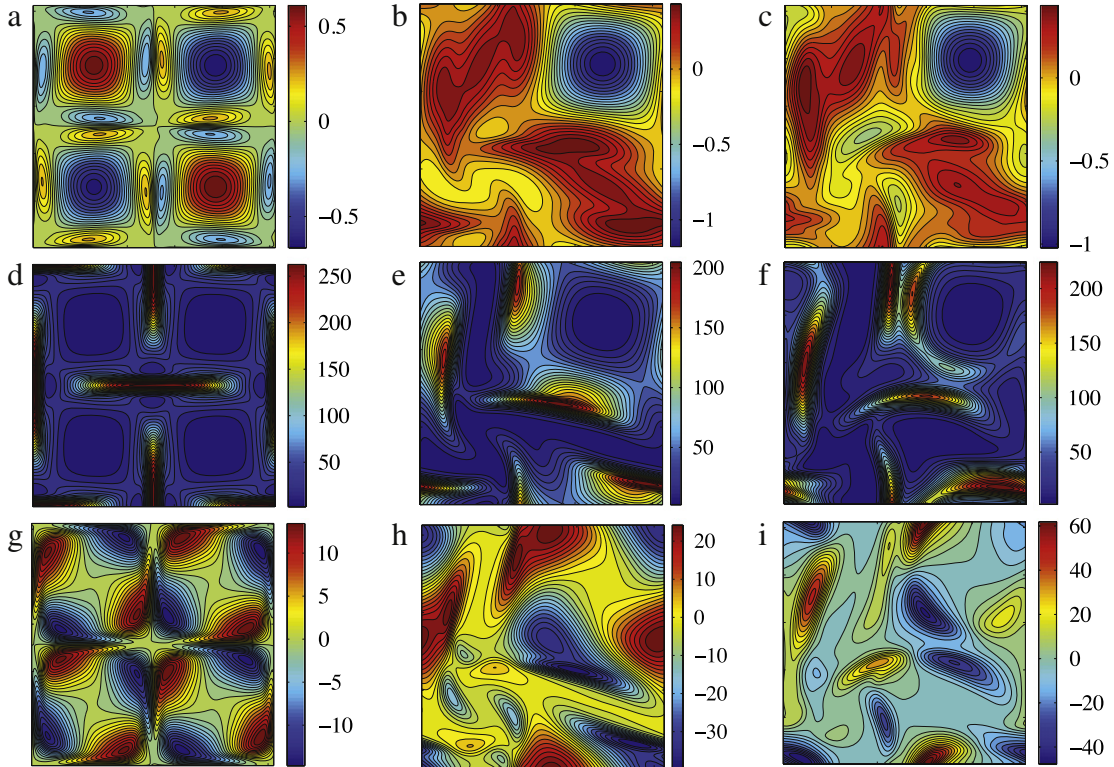


Fig. 4. Contour plots of components of vorticity and polymer stress evolving from random initial data for $Wi = 10$. (a)–(c) Vorticity at $t = 100, 700$ and 1400 , respectively. (d)–(f) $\text{tr } S$ at $t = 100, 700$ and 1400 , respectively. (g)–(i) S_{12} at $t = 100, 700$, and 1400 , respectively.

field, but at $t \approx 1000$ a new higher frequency of oscillation arises as a second transition in the flow occurs. Beyond this time the flow behaves more erratically, with new smaller vortices being formed and destroyed in the flow. Pathlines of the flow at $t = 2450$, are shown in Fig. 5(e). The transition to these new dynamics appears to occur as the vestigial vortex center at $(\pi/2, \pi/2)$ is first destroyed. The dynamics of the vortex centers will be considered further in Section 3.3.

Fig. 5(b) shows the rate of viscous dissipation, $\mathcal{D} = \beta^{-1} \int \int |\nabla \mathbf{u}|^2 \, d\mathbf{x}$ for $Wi = 5, 6$, and 10 for $0 < t < 2000$. These graphs show that \mathcal{D} initially decreases as the solutions go to the near-symmetric states and increases during the transition to asymmetry. For $Wi = 10$ (lower curve) we also see that the onset of the additional flow oscillations is reflected in the viscous dissipation of the fluid. For $Wi = 10$ both u and \mathcal{D} show complicated but near-periodic temporal behavior. In fact, the temporal Fourier spectrum of u (or \mathcal{D}) is controlled by two dominant frequencies; see Fig. 6(d). To explain the decrease in \mathcal{D} as Wi increases we note that as Wi

is increased, $\nabla \mathbf{u} \sim \frac{1}{Wi}$ near extensional points in the flow (as in TS2007).

In 90 of the 100 random trials (for $Wi = 10$) that were performed with initial data given by Eq. (7) the behavior of the flow is as reported above. Namely, after an initial near-symmetric period (roughly $10 < t < 100$) there is a first transition to an asymmetric state with a single-quadrant dominant vortex and at $t \approx 1000$ higher-frequency oscillations arise in the flow (though these do not break the dominance of the single-quadrant vortex). In these trials each of the 4 quadrants contained the preferred vortex with roughly the same proportion. Fig. 6(a)–(c) shows the velocity at a point, $u(\pi/4, \pi/4, t)$, for 5 random trials in which the lower left vortex was preferred. Fig. 6(a) shows the initial behavior: on $0 < t < 10$ the flow rapidly converges to a near steady state (similar to that seen in Fig. 4(a), (c), and (e)), between $100 < t < 200$ the flow becomes asymmetric and there are slow oscillations. Fig. 6(b) shows these slow oscillations for $500 < t < 1000$.

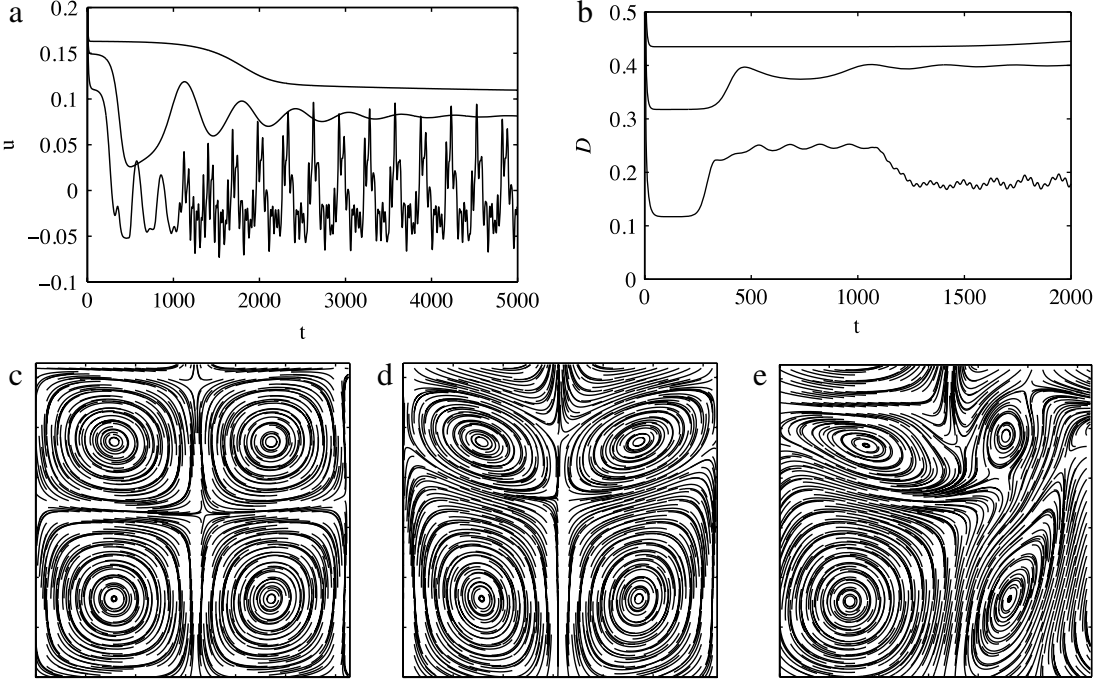


Fig. 5. (a) The first component of the velocity field at a fixed point versus time ($u(t) = u_1(\pi/4, \pi/4, t)$) for $Wi = 5$ (upper curve), 6 (middle curve), and 10 (lower curve). (b) The viscous dissipation versus time for $Wi = 5$ (upper curve), 6 (middle curve), and 10 (lower curve). (c)–(e) Select pathlines of the velocity field at late times for (c) $Wi = 5$ (d) $Wi = 6$ and (e) $Wi = 10$.

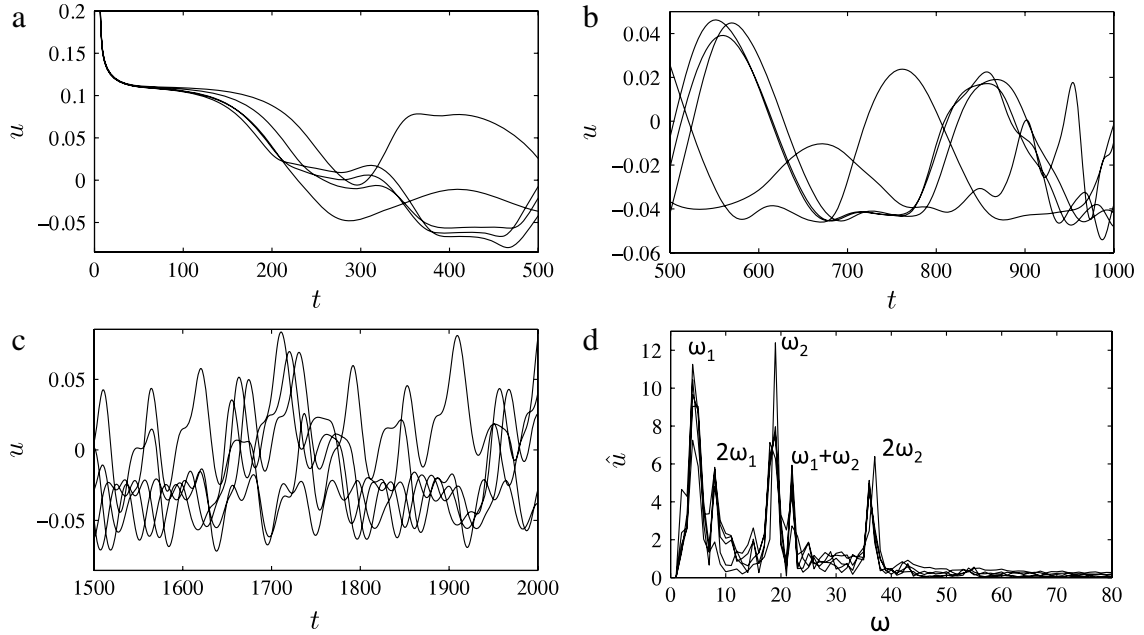


Fig. 6. (a)–(c) The first component of the velocity field at a fixed point versus time ($u(t) = u_1(\pi/4, \pi/4, t)$) for $Wi = 10$ in 5 different trials where lower left vortex is dominant. Note differences in axes. (d) The temporal spectrum of $u(t)$ for $Wi = 10$ from the 5 trials with the transform taken over late times. Two main dominant frequencies ω_1 and ω_2 are highlighted.

Beyond $t \gtrsim 1000$, higher-frequency oscillations emerge, and Fig. 6(c) shows these oscillations on top of the slow oscillations for $1500 < t < 2000$. Fig. 6(d) shows the temporal Fourier transform of u taken over $1000 < t < 2000$. The dominant frequencies ω_1 and ω_2 are marked and all other large activated modes are sums, differences, and harmonics of these two frequencies. These frequencies ω_1 and ω_2 correspond to periods of $\tau_1 \approx 330$ and $\tau_2 \approx 55$. Similar periods are seen for all of the trials with a single-quadrant vortex. The simulations indicate that $\omega_1 \approx 0$ for $Wi = 5$ with ω_1 increasing in Wi . The second frequency ω_2 only arises for

$Wi \gtrsim 9$. These high-frequency oscillations lead to very complicated dynamics in the flow as can be seen in the late-time plots of the vorticity and stress, see Fig. 4(c), (f), and (i).

In 10 of the 100 random trials the dominant vortex does not relax to a single quadrant but instead cycles around the four quadrants. In these two trials the longer period is now $\tau_1 \approx 750$ while the shorter period (still arising as additional higher-frequency oscillations in the flow) was again $\tau_2 \approx 55$. This cycling vortex has significant consequences for mixing in the flow, as will be discussed in Section 4.

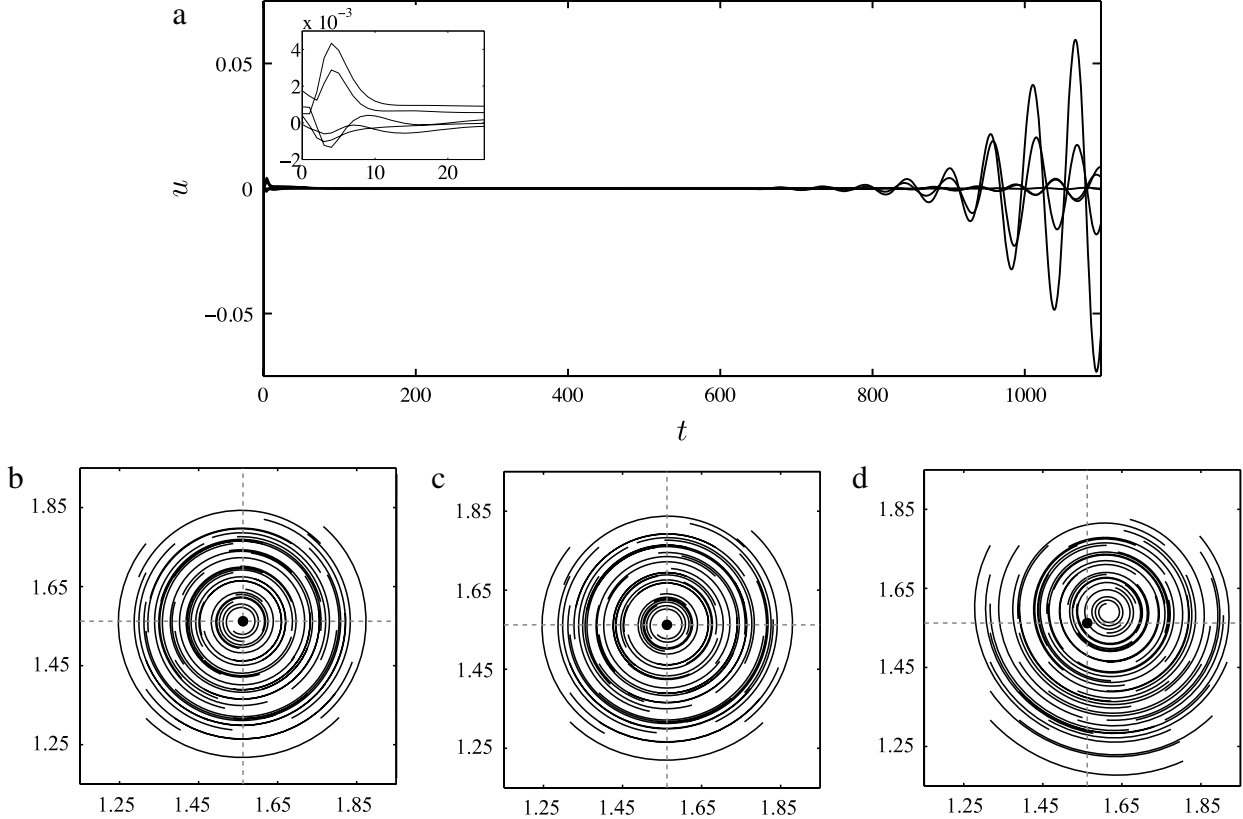


Fig. 7. (a) For $Wi = 10$, plots of the velocity $u_1(\pi/2, \pi/2, t)$ as a function of time for five random trials, the inset plot is a close-up on $0 < t < 25$. (b)–(c) Select pathlines of the velocity at $t = 4, 100$, and $t = 1000$, respectively from one of the random trials. The dotted lines are at $x, y = \pi/2, \pi/2$. Note that at $t = 4$, the dot is very slightly to the upper right of the center of the elliptic point of the pathlines, and at $t = 100$, it has returned to the center.

Changes in background forcing can also cause symmetry-breaking transitions and can be more predictive than changes in the initial data. In fact if one modifies \mathbf{f} to have a slightly dominant quadrant (and then evolves the flow from isotropic initial data) the corresponding vortex will become dominant in the flow evolution. We did not find a way to predict which quadrant will become dominant from the random initial data; indeed the cycling vortex is evidence that prediction is difficult.

3.3. Fixing of elliptic points

The transition to an asymmetric state which occurs as the hyperbolic stagnation point in the flow moves away from the origin was discussed in Section 3.1. We now consider the behavior of the flow at the vortex centers of the background force located at $(\pm\pi/2, \pm\pi/2)$. Fig. 7(a) shows the velocity at $u = u_1(\pi/2, \pi/2, t)$ on $0 < t < 1200$ for 5 trials evolving from random initial data and $Wi = 10$. The inset figure shows a close-up on $0 < t < 25$. In each of these trials the velocity at $(\pi/2, \pi/2)$ is not zero initially, due to the effect of the perturbation, but does converge rapidly toward zero and remains near zero well into the flow evolution. This “pinning” occurs for all values of the Weissenberg number ($Wi \leq 10$ were simulated). For $Wi \lesssim 4.8$ the flow remains symmetric while for $Wi \gtrsim 4.8$ the flow will eventually become asymmetric. Additionally, beyond $Wi \gtrsim 9$ the velocity eventually begins to oscillate beyond some critical time. Fig. 7(b)–(d) show select pathlines of the velocity at $t = 4, 100$, and 1000 , respectively for one of the random trials shown in Fig. 7(a). The dotted lines on each figure are at $x, y = \pi/2$, with a dot at $(\pi/2, \pi/2)$. In Fig. 7(b) the center (or elliptic point) of the vortex is slightly perturbed away from the dot, due to the initial perturbation given in the polymer stress and the resultant

perturbation to the velocity field. In Fig. 7(c) the vortex center coincides with $(\pi/2, \pi/2)$, as prescribed by the steady background force, i.e. the flow locally becomes slaved to the background force. However, by $t = 1000$, in Fig. 7(d) the perturbation has grown sufficiently to move the center of the vortex away from $(\pi/2, \pi/2)$. The second transition in the flow, which occurs for $Wi \gtrsim 9$ and involves the introduction of a higher frequency of oscillations, appears to coincide with the loss of this pinning of the vortex centers to the background force. This apparent “pinning” and subsequent loss of pinning is interesting because there are no obvious symmetries in the equations which account for this initial preservation of symmetry and pinning of the velocity to the background force. It may be evidence of an underlying dynamical structure which ties the behavior of the flow to these components of the background force.

4. Mixing

Although for $5 \lesssim Wi \lesssim 9$ there are time-periodic transient oscillations, the long-time behavior of the flow is steady. Beyond $Wi \approx 9$ the long-time behavior of the flow is time-dependent and hence we consider how the addition of polymer stress affects mixing. We focus here on $Wi = 10$ but consider the effect of increasing Wi in Section 4.4. In the following sections we discuss the mixing between the four quadrants (Section 4.1), effective diffusion (Section 4.2), and compute Lyapunov exponents (Section 4.3). In each of these sections we use passive particles in the flow to quantify mixing.

4.1. Mixing from the four quadrants

Fig. 8 shows how the higher-frequency oscillations in the flow along with symmetry breaking can produce fluid mixing. In [23]

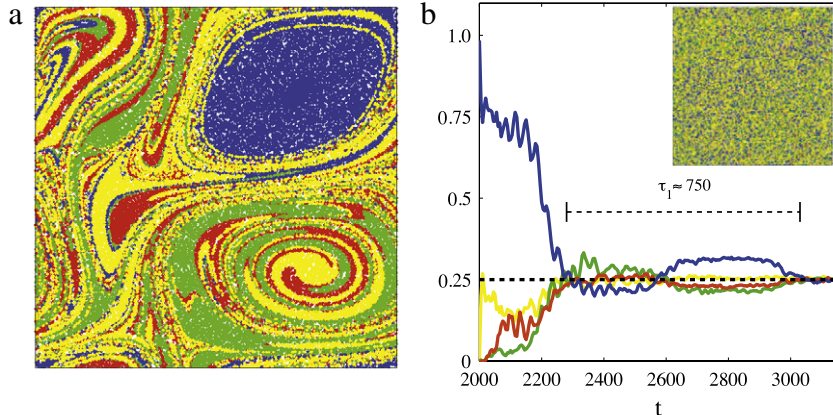


Fig. 8. 4-roll mill mixing: panels (a) and the inset figure in panel (b) show Lagrangian particle distributions from the numerical simulations (using 65,536 particles). Solutions evolve from random initial data, simulation yields stable vortex rotating through all four quadrants. Particles originating in quadrants I (upper right) through IV (lower right) are colored blue, green, red, and yellow, respectively at $t = 2000$. Particle distribution for $Wi = 10$ at $t = 2150$ and $t = 3000$, respectively. (b) The percentage of particles of each color in quadrant I over time, $2000 < t < 3200$. The dashed line at $1/4$ shows the nearly equal representation of all quadrants over long times. τ_1 is the slow period. (For interpretation of the references to colour in this figure legend, the reader is referred to the web version of this article.)

particle mixing was discussed, but not quantified, for a simulation where there was a dominant vortex, and it was shown that outside the dominant vortex there is some mixing due to the transition to asymmetry, and after the onset of the higher-frequency oscillations in the flow the fluid mixes more freely outside the stable vortex (i.e. in 3 of the 4 quadrants). A more global mixer is obtained when the dominant vortex cycles in all four quadrants. Here we consider a simulation where the dominant vortex cycles through all four quadrants. The particles are introduced into the flow at $t = 2000$ in the flow simulation; at this point the symmetry has been broken and higher-frequency oscillations are present. We subdivide the 2π -periodic cell into quadrants, label fluid particles blue, green, red, and yellow (quadrants I through IV, respectively), and track them in the flow, for $t > 2000$. In Fig. 8(a) and inset (b) we see the location of the particle tracers at $t = 2150$ and $t = 3000$ respectively. At $t = 2000$ the dominant vortex is moving between quadrants II and I, cycling clockwise with a full cycle in about 750 time units. Fig. 8(b) shows the percentage of each color in quadrant I as a function of time. We see that for $t \gtrsim 3000$ there is a roughly equal representation of particles from all four quadrants in the upper right quadrant.

4.2. Effective diffusivity

A relevant measure of mixing is how good the flow is at dispersing particles across large length scales. We quantify this by the effective diffusivity of passive particles. To measure this, we tile the plane with periodic copies of the flow \mathbf{u} and allow the passive particles to move freely in \mathbb{R}^2 . Next we compute the mean-square displacement of the particles from the origin over time. Fig. 9(a) and (c) show the location of the particles in two different flows at $t = 1600$ and $t = 1000$ respectively. Fig. 9(a) arises from a simulation where the particles evolve in a flow with a single-quadrant vortex (the lower right one in this case). The 10,000 particles are initially distributed randomly in $[1, 1.05]^2$. The particles avoid the stable vortex which leads to the gaps seen in the figure. Fig. 9(b) is a plot of the mean-square displacement over time, where $\langle X^2 \rangle = \text{mean}(x^2 + y^2)$. The displacement is eventually isotropic and the rate of growth of the x displacement is nearly equal to the rate of growth of the y displacement; the correlation between x and y shows very little growth. The effective diffusivity (or rate of growth of $\langle X^2 \rangle$, divided by 4) is approximately 0.025.

Fig. 9(c) shows results from a simulation where the particles evolve in a flow with a clockwise-cycling dominant vortex. Here there are no gaps in the particle distribution (as there are no visible

trapping regions in the flow); however the displacement is no longer isotropic, but rather is much greater along the line $y = x$. Fig. 9(d) again displays the mean-square displacement over time and we see that the correlation $\langle xy \rangle$ is no longer zero. In this case the diffusivity tensor D , given by $2D_{ij} = \langle x_i x_j \rangle$, is

$$D = \begin{pmatrix} 0.044 & 0.039 \\ 0.039 & 0.044 \end{pmatrix}.$$

The eigenvalues of D are 0.083 with eigenvector $(0.707 \ 0.707)^T$; and 0.005 with eigenvector $(0.707 - 0.707)^T$. The larger eigenvalue gives the diffusivity along the line $y = x$, and is larger than the isotropic value (from Fig. 9(a)) by a factor of nearly four. Thus large-scale transport is more effective for the type of solution in Fig. 9(c), but also much more anisotropic.

4.3. Lyapunov exponents and variance decay

4.3.1. Background

The effective diffusivity described in Section 4.2 is useful when one has an array of rolls and it is desired to measure transport across large scales. If the system consists of a single four-roll mill, however, we need to resort to a more refined measure of mixing quality that is better suited to chaotic mixing [38,39]. It has long been appreciated that finite-time Lyapunov exponents characterize mixing in smooth flows. The exponents describe the rate of separation of nearby trajectories from a given initial condition. Different initial conditions typically lead to different finite-time Lyapunov exponents, since they depend on time, though at large times they all converge to the same value for a given invariant region. We can then speak of a probability distribution function (PDF) of finite-time Lyapunov exponents by starting trajectories at many different points. This PDF is obtained numerically and averaged as described below to obtain the decay rate of the variance of a passive scalar field advected by the flow (see [40–45]).

The connection between Lyapunov exponents and mixing arises from the stretching nature of chaotic flows: in incompressible flows stretching necessarily implies compression in another direction, and this compression amplifies gradients of a passive scalar. Large gradients cause mixing to proceed at an accelerated rate, since they greatly amplify the effect of molecular diffusion.

4.3.2. Computing the PDF of Lyapunov exponents

To compute a PDF of Lyapunov exponents, we first need to select a set of particle trajectories that belong to a single invariant chaotic

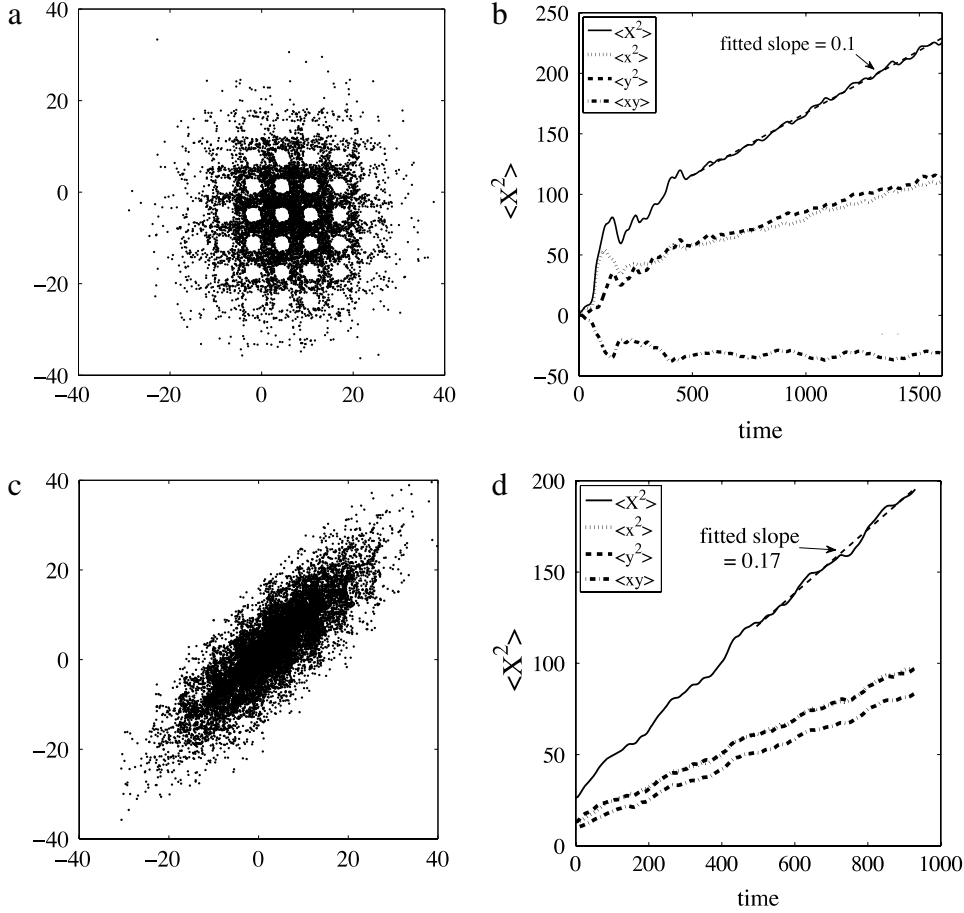


Fig. 9. (a) $Wi = 10$ particle distribution in the plane for simulation with single stable vortex at $t = 1600$. (b) Mean-square displacement of particles over time. Diffusion is isotropic (although avoids the stable vortex) and has a diffusion rate ≈ 0.10 . (c) $Wi = 10$ particle distribution in the plane for simulation with rotating vortex at $t = 1000$. (d) Mean-square displacement of particles over time. Diffusion is much greater along $y = x$ axis.

region. In our case, this region is determined by initializing 10,000 particles randomly distributed in $[1, 1.05]^2$ at $t = 2000$, i.e. well into the flow evolution, after the onset of the higher-frequency oscillations. In the chosen simulation there is a dominant vortex in the lower right quadrant. The particles are constrained to a single 2π -periodic box and after $t = 1100$ time units have filled up the mixing region and lost their initial correlations. Fig. 10(a) shows the position of these particles at $t = 3100$.

Next, we obtain the positive finite-time Lyapunov exponent by evolving a small stencil of points around a reference trajectory. We then calculate the Cauchy–Green deformation tensor by finite-differencing the stencil, and use the tensor to find the Lyapunov exponents [39]. Two exponents are obtained from the rate of growth or decay of the two eigenvalues of the Cauchy–Green tensor (by convention, this rate is divided by two). Because of incompressibility, the exponents always have the same magnitude but with opposite signs, so we may focus on the positive exponent. Care is taken to ensure that the points in the stencil do not get so far apart that the linear approximation breaks down.

Fig. 10(b) shows a histogram of the positive finite-time Lyapunov exponents λ_1 after 500 time units from the start of the trajectories, with a Gaussian fit overlayed. The mean is converging to $\bar{\lambda}_1 \approx 0.014$, as shown in Fig. 10(c). In that figure we show a large-time fit to $\bar{\lambda}_1 + \text{const.}/\sqrt{t}$ used to estimate the time-asymptotic value $\bar{\lambda}_1$ of the mean finite-time Lyapunov exponent, as in [46,47].

A plot of σ^{-2} given in Fig. 10(d) shows that $\sigma \sim t^{-1/2}$ for large times, the form expected for a Gaussian distribution arising from the additive process that yields the Lyapunov exponents. Note that

we assume that the Gaussian fit of the PDF is sufficient to estimate the decay rate of variance of the passive scalar field. We do not have sufficient data to attempt to find a more accurate form for the Cramér function [40–45].

4.3.3. Decay rate of variance of the passive scalar field

From the mean $\bar{\lambda}_1 \approx 0.014$ and standard deviation $\sigma = (\alpha/t)^{1/2}$, we can estimate the decay rate γ of the variance of a passive tracer stirred by our chaotic flow, following the ‘local stretching theory’ [40–43,45]. In this theory, which has been verified to a high degree of accuracy for variance decay [44], the PDF of finite-time Lyapunov exponents is used to average the decay of a representative ‘blob’ of passive scalar. The long-time decay rate is then extracted using the saddle-point method. The ratio $\bar{\lambda}_1/\alpha \approx .467 < 1$ indicates that the variance decay rate is dominated by ‘zero stretching’ orbits, which implies that

$$\gamma = \bar{\lambda}_1^2/2\alpha \approx 0.014^2/(2 \times 0.03) \approx 0.0033. \quad (8)$$

(See for instance Eq. (61) in [43] with $\alpha = 1$.) Thus, variance decays on time-scales of $1/0.0033 \approx 300$ time units. The variance decay rate $\gamma \approx 0.0033$ is considerably slower than the infinite-time Lyapunov exponent $\bar{\lambda}_1 \approx 0.014$. This is typical of a ‘fluctuation-dominated’ system such as this one (with $\bar{\lambda}_1/\alpha < 1$): orbits with low stretching values are weighed heavily and come to dominate, thereby slowing the decay rate. This type of behavior is also observed in simple micromixers [43].

The process is repeated for a simulation with a cycling vortex. In this case the particles fill up the entire domain $[0, 2\pi]^2$. The

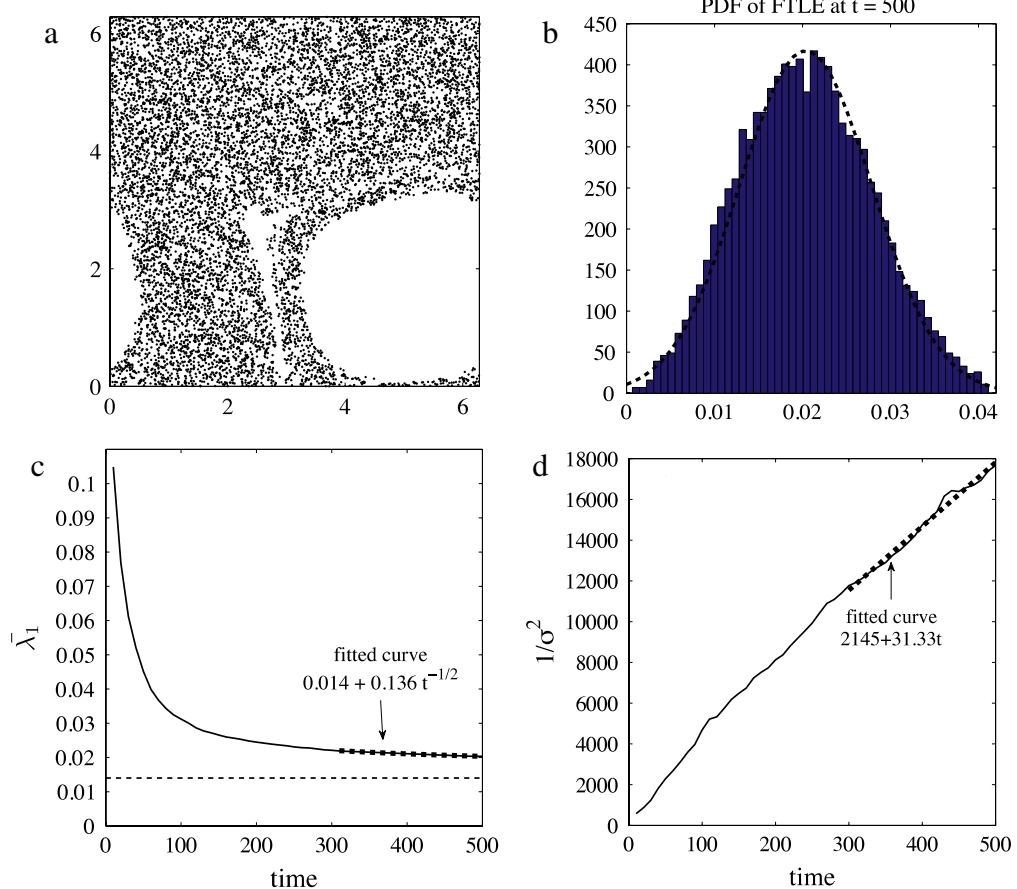


Fig. 10. (a) Initial mixing region containing 10,000 particles which evolved for $t = 1100$ time units. Particles were initially randomly distributed in $[1, 1.05]^2$. (b) Histogram of largest eigenvalue after evolving for 500 time units from initial distribution in (a), as well as a Gaussian fit. (c) Plot of $\bar{\lambda}_1$ the largest eigenvalue over time. (d) Plot of σ the standard deviation of the distribution of the largest eigenvalue over time: $\sigma \sim t^{-1/2}$.

mean Lyapunov exponent $\bar{\lambda}_1 \approx 0.0093$ is smaller than in the case of a dominant vortex. For large t the standard deviation is approximately $\sigma \approx (\alpha/t)^{1/2}$ with $\alpha \approx 0.029$. The net decay rate of variance computed as in (8) is then 0.0015, about half the value for the fixed vortex above. That the decay rate is smaller, and thus the flow a slower mixer, for the situation with more ‘global’ chaotic behavior is not too surprising: there is no reason to expect a faster decay just because the chaos is global. For most practical applications, it is preferable to adopt the global mixing of the cycling vortex in spite of the slower decay rate.

4.4. Higher Weissenberg number

The behavior of the flow at higher Wi is qualitatively similar to $Wi = 10$: there is a preferred vortex which is either stable in a single quadrant or else it cycles through the four quadrants. However, there are some differences in the nature of the flow. Fig. 11(a) shows the velocity $u_1(3\pi/8, 3\pi/8, t)$ for $Wi = 10, 12, 15, 20, 30$ over $1800 < t < 3000$. For $Wi = 10$ the velocity appears to be quasi-periodic, but for $Wi = 12, 15$ the flow seems to become periodic. Fig. 11(b) shows the spectrum for the time-series for $Wi = 12$ which clearly indicates periodic dynamics. Beyond $Wi \gtrsim 20$ the flow begins to exhibit more random behavior, as reflected by a more broad-band spectrum, Fig. 11(c). Computations of effective diffusivity show that the rate of diffusion decreases in Wi over the range $10 < Wi < 30$. Fig. 11(d) shows computations of the finite-time Lyapunov exponents for $Wi = 10, 12, 15, 20$, and 30; the figure shows $\bar{\lambda}_1$ and the insets show the converged values for these exponents, fit to a curve $\bar{\lambda}_1 + \text{const.} \cdot \frac{1}{\sqrt{t}}$ as in Section 4.3. It

is non-monotonic in Wi , with $Wi = 12$ having the largest value. The higher Wi dynamics and consequences for mixing require further study. There is no reason to expect monotonicity in Wi in such flow statistics as effective diffusivity or Lyapunov exponents, but the transition from quasi-periodic to periodic to aperiodic dynamics is puzzling and further evidence that this system is very complicated.

5. Conclusions

The simulations described above are consistent with experiments on viscoelastic instabilities in cross-channel flows [20], and begin to give some information about the nature of these instabilities. For sufficiently large Weissenberg number the polymer stress grows and concentrates along the outgoing streamlines of the extensional point in the flow. The polymer stress diffusion added in our simulations both bounds and smooths the polymer stress allowing for long-time simulations. Also along the incoming and outgoing streamlines additional vortices appear in the flow. Given a small perturbation in the initial data which breaks the symmetry of the initial four-roll mill structure of the flow, the polymer stress will eventually begin to reconfigure, leading to asymmetric flow states. The resulting velocity may have a largest dominant vortex with the remaining vortices smaller in magnitude. Due to the rearrangement there is enhanced fluid mixing in the regions with the smaller vortices.

During this process there are (up to) three time periods of interest. The first is the initial phase where the polymer stress is growing (for $Wi \gtrsim 1$). According to the local model in TS2007

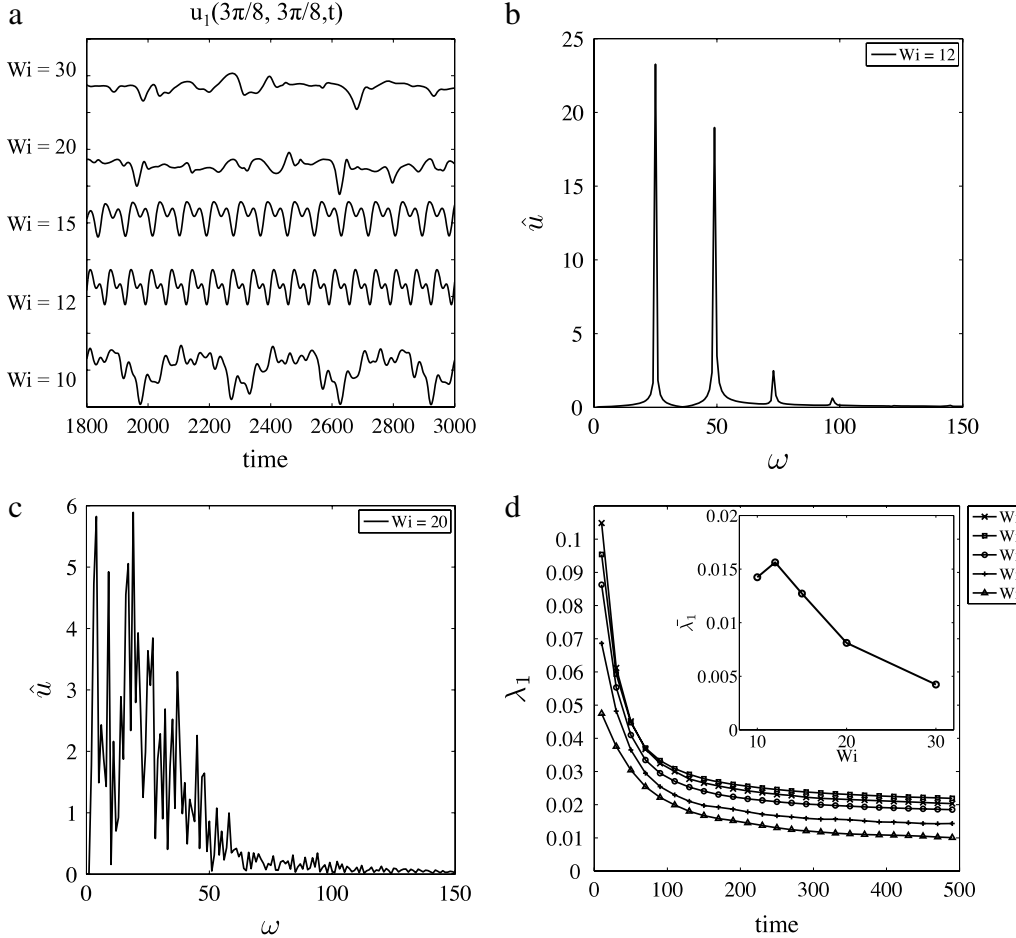


Fig. 11. (a) $u_1(3\pi/8, 3\pi/8, t)$ for $Wi = 10, 12, 15, 20, 30$ over $1800 < t < 3000$. Mean velocity is shifted vertically for clarity. (b, c) The temporal spectrum of $u(t)$ for $Wi = 12, 20$. (d) Plot of λ_1 over time for $Wi = 10, 12, 15, 20, 30$. Inset plot gives converged value of λ_1 .

the polymer stress grows exponentially in time at the extensional points in the flow and will become unbounded, unless there is a cut-off mechanism such as the finite extensibility of polymer coils or stress diffusion. The second period of interest (for $Wi \gtrsim 4.9$) follows after a period of relatively steady symmetric behavior. The flow becomes asymmetric with slow oscillations in the velocity field (with these oscillations increasing in Wi) which dampen out in time for $4.9 \lesssim Wi \lesssim 9$ as the flow becomes steady once again, though in an asymmetric configuration. For $Wi \gtrsim 9$, the loss of pinning of a vortex center previously fixed by the background force coincides with the onset of a new higher frequency of oscillations in the flow and more complicated flow behaviors are seen with the continual destruction and creation of vortices. This new flow state leads to significant mixing in the flow. For $Wi = 10$ there is also a set of stable solutions where the preferred vortex cycles clockwise (or counter-clockwise) throughout the four quadrants.

The onset of these higher oscillations also leads to significant mixing in the fluid. The mixing can be quantified by measuring effective diffusions of particle tracers and Lyapunov exponents. Increasing Wi does not lead in a monotone fashion to more complicated flow structures or more mixing. In fact there appears to be a transition from quasi-periodic flow dynamics (for $Wi = 9, 10$) to periodic dynamics ($Wi = 12, 15$) and then aperiodic dynamics ($Wi \gtrsim 20$). The higher Wi dynamics will be investigated in future work. Clearly, the full set of possible states for this system is still largely unknown. We do see a forward bifurcation to a multi-stable steady state for sufficiently large Weissenberg number ($Wi \gtrsim 4.8$), as seen by Arratia et al. in [20]. In our

simulations the particular asymmetry is chosen by the initial data, although the exact selection mechanism is unclear.

The FENE-P model [48] also shows similar transitions and flow states. More detailed studies are ongoing. Future work includes investigations into the origins of the instability via bifurcation and stability analysis. More complicated behavior is also seen upon increasing the degrees of freedom by considering a 16-roll background force; this work is ongoing. Finally, other modes of instability are available in three dimensions and we anticipate yet richer behavior there [49].

Acknowledgments

The authors would like to thank Steve Childress for many stimulating years of discussion and collaboration. Additionally, the authors would like to thank E. Wolfson at the Courant Institute for assistance. The first author was partially supported by NSF grant DMS-0757813. The second author was partially supported by DOE grant DE-FG02-88ER25053 and NSF grant DMS-0652795.

Appendix A. Numerical method

We solve the Stokes–Oldroyd-B system with polymer stress diffusion, (1) and (2), with a pseudo-spectral method, [50]. The polymer stress \mathbf{S} is evolved using a second-order Adams–Bashforth–Crank–Nicholson method. The initial data (symmetric positive definite) for \mathbf{S} is prescribed, and given \mathbf{S} , the Stokes equation, Eq. (1), is inverted in Fourier space for \mathbf{u} . Given \mathbf{u} , the nonlinearities of the polymer stress evolution, Eq. (2), are evaluated using a

smooth filter which is applied in Fourier space before the quadratic terms are multiplied in real space; see [51] for details. The polymer stress equation, Eq. (2), is considered in the form

$$\partial_t \mathbf{S} = v_p \Delta \mathbf{S} + N(\mathbf{S}, \mathbf{u}),$$

where $N(\mathbf{S}, \mathbf{u}) = -\mathbf{u} \cdot \nabla \mathbf{S} + (\nabla \mathbf{u} \cdot \mathbf{S} + \mathbf{S} \cdot \nabla \mathbf{u}^T) - \frac{1}{Wi}(\mathbf{S} - \mathbf{I})$. The polymer stress is then discretized on the Fourier transform side

$$\begin{aligned} \frac{\hat{\mathbf{S}}^{n+1} - \hat{\mathbf{S}}^n}{\Delta t} &= -v_p |k|^2 \frac{\hat{\mathbf{S}}^{n+1} + \hat{\mathbf{S}}^n}{2} \\ &+ \frac{1}{2}[3\hat{N}(\mathbf{S}^n, \mathbf{u}^n) - \hat{N}(\mathbf{S}^{n-1}, \mathbf{u}^{n-1})]. \end{aligned}$$

Note that $v_p \equiv 0$ will yield the typical second-order Adams-Bashforth scheme. We find that positive definiteness is maintained in all of our simulations and the time-stepping was verified to have second-order accuracy. For $Wi \leq 10$, with $v_p = 10^{-3}$ a spatial discretization of $n^2 = 256^2$ is sufficient to resolve the spatial accuracy to $\mathcal{O}(10^{-12})$, for the long times necessary for this study. For $Wi > 10$ we scale $v_p = \frac{0.1}{Wi}$, and there is some loss of accuracy, however for $Wi \leq 30$, the spatial accuracy is still resolved to $\mathcal{O}(10^{-4})$ with the diffusion scaled as above.

An additional component to our numerical study is the need to track particles in the flow. We use second-order spatial interpolation to obtain the velocity field between grid cells, and update the particles with this velocity using a second-order method.

Appendix B. Choice and calibration of model

In this study we use the Stokes–Oldroyd-B system with polymer stress diffusion given by Eqs. (1) and (2). This model differs from the standard Stokes–Oldroyd-B model by the addition of the polymer stress diffusion term $v_p \Delta \mathbf{S}$. In the derivation of the Oldroyd-B model from kinetic theory [26] it is assumed that the spatial diffusion of the probability density function is quite small compared with the diffusion in phase space, and hence this term is usually ignored. It is included here in an approximate form. In [36] it was shown that a similar modification of the polymer stress equation can be justified from microscopic principles (at least for steady solutions) and will yield smooth solutions for the polymer stress as long as the polymer stress remains bounded. In our simulations we see that the addition of this term keeps the polymer stress bounded and smooth dynamically as well, whereas for $v_p = 0$ the polymer stress will grow at least exponentially at extensional points in the flow for sufficiently large Weissenberg number. We choose the size v_p so that the solutions to the Stokes–Oldroyd-B model with polymer diffusion compare well with solutions which maintain finite extensibility. These solutions come from the FENE-P model described below.

FENE (Finitely Extensible Nonlinear Elastic) models are a model of viscoelastic fluids which incorporate finite extension of polymer coils in their derivation. In the FENE model [27] the response of a polymer coil is no longer a linear Hookean spring, as for Oldroyd-B, but is given by Warner's force law [52]

$$\mathbf{F} = \frac{\kappa \mathbf{R}}{1 - (\mathbf{R}^2/\ell^2)},$$

where κ is the spring constant, \mathbf{R} is the end to end vector representing the polymer coil, and ℓ is the maximum allowed extension length. This force law penalizes distension of the polymer coils (given by the end to end vector \mathbf{R}). However, unlike Oldroyd-B, this model does not close under the macroscopic assumptions and therefore computations of the full FENE model require a coupling of the microscopic scale, to simulate the polymers, with the macroscopic flow field. These computations are

prohibitively expensive in general. A simple way to obtain a closed macroscopic model is via pre-averaging, i.e. choosing a force law of the form

$$\mathbf{F} = \frac{\kappa \mathbf{R}}{1 - (\langle \mathbf{R} \rangle^2/\ell^2)},$$

where the brackets indicate taking the average over the probability density function of \mathbf{R} . This yields the closed macroscopic FENE-P model [48] which does give a finite extension length. This artificial cut-off of $\text{tr } \mathbf{S}$, however does not smooth the polymer stress sufficiently to make long-time computations reasonable, [28].

Simulations of FENE-P were done in TS2007 in a 2D periodic extensional flow with the four-roll mill geometry, to compare directly with the similar results for the standard Stokes–Oldroyd-B model. In these simulations $\text{tr } \mathbf{S}$ remained bounded for all Weissenberg number. However singularities still arise exponentially in time in the polymer stress gradient for sufficiently large Weissenberg number. These singularities appeared as either cusps ($1/2 \lesssim Wi \lesssim 1$) or corners ($Wi \gtrsim 1$). Although the FENE-P model does maintain a finite polymer stress at all time, the singularities in the polymer stress gradients cause the same numerical difficulties as the Stokes–Oldroyd-B model for long-time simulations of the dynamic equations, which suggests a potentially non-physical cut-off mechanism.

We note that the use of $v_p > 0$ does not modify the polymer stress significantly outside a small region of the extensional points in the flow. In TS2007 it was observed that in the Oldroyd-B model for sufficiently large Wi the polymer stress is diverging, but it was also noted that $\text{tr } \mathbf{S}$ gets large on a set of exponentially shrinking measure. Outside of this set $\text{tr } \mathbf{S}$ does reach a steady state. The width of the divergent region decreases exponentially in time and the net force from this region also decreases in time. This may explain why the unsteady region (with $v_p = 0$) has a decreasing effect on the flow. Given this observation it seems more important that the polymer stress in the modified system ($v_p > 0$) behaves qualitatively like the polymer stress from the Stokes–Oldroyd-B system outside a small region near the stagnation point, than that the exact details of the polymer stress match very close to the stagnation point.

To demonstrate the effect of the parameter v_p on the stress, in Fig. 12(a) we plot $S_{11}(\pi, x)$ at $t = 10$ for $Wi = 5.0$, and for $v_p = 10^{-2}, 10^{-3}, 10^{-4}$. These simulations used $\mathbf{S}(0) = \mathbf{I}$ as the initial condition and the steady background forcing given in Eq. (6). The polymer stress has reached an approximate steady state at this time for $v_p > 0$. We see that as the diffusion decreases the peak of the polymer stress increases and the polymer stress is more concentrated at the stagnation point ($y = \pi$).

In Fig. 12(b) we compare $S_{11}(\pi, y)$ at $t = 10$ for the case of no diffusion ($v_p = 0$), $v_p = 10^{-3}$, and FENE-P with length cut-off $\ell^2 = 50$. We see that the polymer stress with $v_p = 10^{-3}$ is a nice match to the FENE-P simulation in terms of both the maximum value and the overall spread of the polymer stress about the stagnation point at $y = \pi$. We note that although there are similarities in the behavior of the stress with the FENE-P cut-off and with the numerical diffusion, these are distinct modifications to the model which arise from different microscopic origins and have different effects on the flow in general. For example; the FENE model results in shear-rate-dependence in the normal stresses at high Wi , whereas the numerical diffusivity of the Oldroyd-B model does not affect the quadratic scaling with Wi in homogeneous flows.

By examining the decay of the Fourier spectrum (not shown) for $\hat{S}_{11}(\pi, k)$, $Wi = 5.0$ at $t = 10$, for each level of diffusion with $n = 256^2$ spatial grid-points, we see that both $v_p = 10^{-2}$ and $v_p = 10^{-3}$ are well resolved at $n = 256^2$, whereas to obtain the same amount of accuracy for $v_p = 10^{-4}$ one would have to significantly

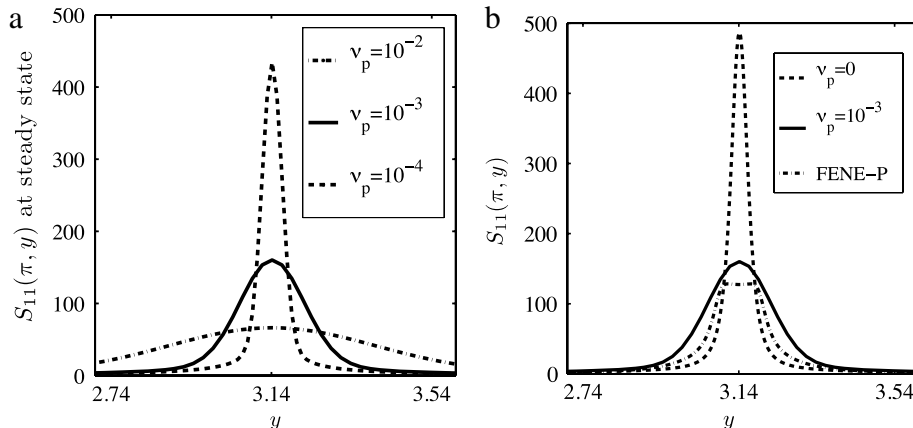


Fig. 12. (a) Plot of $S_{11}(\pi, y)$ at steady state for $\text{Wi} = 5.0$ comparing different amounts of diffusion, ranging from $v_p = 10^{-2}, 10^{-3}, 10^{-4}$. (b) Plot of $S_{11}(\pi, y)$ at $t = 10$ for $\text{Wi} = 5.0$ comparing no diffusion ($v_p = 0$), FENE-P (with length cut-off $\ell^2 = 50$), and diffusion $v_p = 10^{-3}$.

increase n , and hence computation time. The long-time simulations we are after can be accomplished reasonably using $n^2 = 256^2$ and hence the choice of $v_p = 10^{-3}$ is sufficient both for numerical considerations and for the favorable comparison with FENE-P.

References

- [1] A. Groisman, V. Steinberg, Elastic turbulence in a polymer solution flow, *Nature* 405 (2000) 53–55.
- [2] A. Groisman, V. Steinberg, Efficient mixing at low Reynolds numbers using polymer additives, *Nature* 410 (2001) 905–908.
- [3] A. Groisman, V. Steinberg, Elastic turbulence in curvilinear flows of polymer solutions, *New J. Phys.* 4 (2004) 74437.
- [4] E.M. Purcell, Life at low Reynolds number, *Amer. J. Phys.* 45 (1977) 3–11.
- [5] A. Groisman, S. Quake, A microfluidic rectifier: anisotropic flow resistance at low Reynolds numbers, *Phys. Rev. Lett.* 92 (2004) 094501.
- [6] J. Teran, L. Fauci, M. Shelley, Peristaltic pumping and irreversibility of a Stokesian viscoelastic fluid, *Phys. Fluids* 20 (2008) 073101.
- [7] E. Shaqfeh, S.J. Muller, R.G. Larson, A purely elastic transition in Taylor–Couette flow, *Rheol. Acta* 28 (1989) 499.
- [8] G.H. McKinley, J.A. Byars, R.A. Brown, R.C. Armstrong, Observations on the elastic instability in cone-and-plate and parallel-plate flows of a polyisobutylene Boger fluid, *J. Non-Newton. Fluid Mech.* 40 (1991) 201.
- [9] A. Oztekin, R.A. Brown, Instability of a viscoelastic fluid between rotating parallel disks: analysis for the Oldroyd-B fluid, *J. Fluid Mech.* 255 (1993) 473.
- [10] J.A. Byars, A. Öztekin, R.A. Brown, G.H. McKinley, Spiral instabilities in the flow of highly elastic fluids between rotating parallel disks, *J. Fluid Mech.* 271 (1994) 173.
- [11] Peyman Pakdel, Gareth H. McKinley, Elastic instability and curved streamlines, *Phys. Rev. Lett.* 77 (12) (1996) 2459–2462.
- [12] E. Shaqfeh, Purely elastic instabilities in viscometric flows, *Annu. Rev. Fluid Mech.* 28 (1996) 129.
- [13] G.H. McKinley, T. Sridhar, Filament-stretching rheometry of complex fluids, *Annu. Rev. Fluid Mech.* 34 (2002) 375.
- [14] R.G. Owens, T.N. Phillips, Computational Rheology, Imperial College Press, 2002.
- [15] N. Phan-Thien, Coaxial-disk flow of an Oldroyd-B fluid: Exact solution and stability, *J. Non-Newton. Fluid Mech.* 13 (1983) 325.
- [16] J.J. Magda, R.G. Larson, A transition occurring in ideal elastic liquids during shear flow, *J. Non-Newton. Fluid Mech.* 30 (1988) 1.
- [17] D.E. Smith, H.P. Babcock, S. Chu, Single-polymer dynamics in steady shear flow, *Science* 283 (1999) 1724.
- [18] J.P. Rothstein, G.H. McKinley, The axisymmetric contraction expansion: the role of extensional rheology on vortex growth dynamics and the enhanced pressure drop, *J. Non-Newton. Fluid Mech.* 98 (2001) 33.
- [19] C. Schroeder, H. Babcock, E. Shaqfeh, S. Chu, Observation of polymer conformation hysteresis in extensional flow, *Science* 301 (2003) 1515.
- [20] P.E. Arratia, C.C. Thomas, J. Diorio, J.P. Gollub, Elastic instabilities of polymer solutions in cross-channel flow, *Phys. Rev. Letters* 96 (2006) 144502.
- [21] A. Groisman, M. Enzelberger, S. Quake, Microfluidic memory and control devices, *Science* 300 (2003) 955.
- [22] L.E. Rodd, T.P. Scott, D.V. Boger, J.J. Cooper-White, G.H. McKinley, The inertio-elastic planar entry flow of low-viscosity elastic fluids in micro-fabricated geometries, *J. Non-Newton. Fluid Mech.* 129 (2005) 1.
- [23] B. Thomases, M. Shelley, Transition to mixing and oscillations in a Stokesian viscoelastic flow, *Phys. Rev. Lett.* 103 (2009) 094501.
- [24] L. Xi, M. Graham, A mechanism for oscillatory instability in viscoelastic cross-slot flow, *J. Fluid Mech.* 622 (2009) 145–165.
- [25] S. Berti, A. Bistagnino, G. Boffetta, A. Celani, S. Musacchio, Two-dimensional elastic turbulence, *Phys. Rev. E* 77 (2008) 055306.
- [26] M. Doi, S. Edwards, The Theory of Polymer Dynamics, Oxford University Press, New York, 1986.
- [27] R.G. Larson, The Structure and Rheology of Complex Fluids, Oxford University Press, 1998.
- [28] B. Thomases, M. Shelley, Emergence of singular structures in Oldroyd-B fluids, *Phys. Fluids* 19 (2007) 103103.
- [29] E.J. Hinch, Mechanical models of dilute polymer solutions in strong flows, *Phys. Fluids* 20 (1977) S22–S30.
- [30] M. Chertkov, Polymer stretching by turbulence, *Phys. Rev. Lett.* 84 (20) (2000) 4761–4764.
- [31] Jean-Luc Thiffeault, Finite extension of polymers in turbulent flow, *Phys. Lett. A* 308 (5–6) (2003) 445–450.
- [32] M. Renardy, A comment on smoothness of viscoelastic stresses, *J. Non-Newton. Fluid Mech.* 138 (2006) 204–205.
- [33] C.-Y. Lu, P.D. Olmsted, R.C. Ball, Effects of nonlocal stress on the determination of shear banding flow, *Phys. Rev. Lett.* 84 (2000) 642.
- [34] E.J. Hinch, Uncoiling a polymer molecule in a strong extensional flow, *J. Non-Newton. Fluid Mech.* 54 (1994) 209.
- [35] J.M. Rallison, Dissipative stresses in dilute polymer solutions, *J. Non-Newton. Fluid Mech.* 68 (1996) 61.
- [36] A.W. El-Kareh, L.G. Leal, Existence of solutions for all Deborah numbers for a non-Newtonian model modified to include diffusion, *J. Non-Newton. Fluid Mech.* 33 (1989) 257.
- [37] J.M. Rallison, E.J. Hinch, Do we understand the physics in the constitutive equation? *J. Non-Newton. Fluid Mech.* 29 (1988) 37–55.
- [38] H. Aref, Stirring by chaotic advection, *J. Fluid Mech.* 143 (1984) 1–21.
- [39] J.M. Ottino, The Kinematics of Mixing: Stretching, Chaos, and Transport, Cambridge University Press, Cambridge, UK, 1989.
- [40] T.M. Antonsen Jr., Z. Fan, E. Ott, E. Garcia-Lopez, The role of chaotic orbits in the determination of power spectra, *Phys. Fluids* 8 (11) (1996) 3094–3104.
- [41] E. Balkovsky, A. Fouxon, Universal long-time properties of Lagrangian statistics in the Batchelor regime and their application to the passive scalar problem, *Phys. Rev. E* 60 (4) (1999) 4164–4174.
- [42] J. Sukhatme, R.T. Pierrehumbert, Decay of passive scalars under the action of single scale smooth velocity fields in bounded two-dimensional domains: from non-self-similar probability distribution functions to self-similar eigenmodes, *Phys. Rev. E* 66 (November) (2002) 056032.
- [43] Jean-Luc Thiffeault, Scalar decay in chaotic mixing, in: J.B. Weiss, A. Provenzale (Eds.), Transport and Mixing in Geophysical Flows, in: Lecture Notes in Physics, vol. 744, Springer, Berlin, 2008, pp. 3–35.
- [44] Y.-K. Tsang, T.M. Antonsen Jr., E. Ott, Exponential decay of chaotically advected passive scalars in the zero diffusivity limit, *Phys. Rev. E* 71 (2005) 066301.
- [45] P.H. Haynes, J. Vanneste, What controls the decay of passive scalars in smooth flows? *Phys. Fluids* 17 (2005) 097103.
- [46] Xian Zhu Tang, Allen H. Boozer, Finite time Lyapunov exponent and advection-diffusion equation, *Physica D* 95 (1996) 283–305.
- [47] Jean-Luc Thiffeault, P.J. Morrison, The twisted top, *Phys. Lett. A* 283 (5–6) (2001) 335–341.
- [48] R.B. Bird, P.J. Dotson, N.L. Johnson, Polymer solution rheology based on a finitely extensible bead-spring chain model, *J. Non-Newton. Fluid Mech.* 7 (1980) 213–235.
- [49] R.G. Larson, S.J. Muller, E.S.G. Shaqfeh, A purely elastic instability in Taylor–Couette flow, *J. Fluid Mech.* 218 (1990) 573–600.
- [50] Roger Peyret, Spectral Methods for Incompressible Viscous Flow, Springer, New York, 2002.
- [51] T.Y. Hou, R. Li, Computing nearly singular solutions using pseudo-spectral methods, *J. Comput. Phys.* 226 (2007) 379–397.
- [52] H.R. Warner, Kinetic theory and rheology of dilute suspensions of finitely extensible dumbbells, *Ind. Eng. Chem. Fundam.* 11 (1972) 379–387.